RESEARCH

Structural and Physical Comparison Between CS/PVP Blend and CS/PVP/Sr-Hexaferrite Nanocomposite Films

Rania Ramadan[1] · A. M. Ismail[2]

Abstract

CS/PVP blend embedded by Sr-hexaferrite nanoparticles as a novel composite material to improve the optical and magnetic properties of composite samples. This work aimed to study and compare the functional and physical properties of CS/PVP film after and before adding $SrFe_{12}O_{19}$ with different weight percentages to form nanocomposite film with chemical formula CS/PVP/x Wt% $SrFe_{12}O_{19}$; x = 1, 3, 5 and 7. $SrFe_{12}O_{19}$ was prepared successfully by using citrate auto-combustion methods, then added to CS/PVP blend with different weight percentages. XRD shows the formation of Sr-hexaferrite in a single phase with an average crystallite size 44 nm. The semi-crystalline nature of CS/PVP film decreases with the addition of Sr-hexaferrite. FTIR displays the interaction between CS/PVP and $SrFe_{12}O_{19}$ by changing the intensity and broadening the OH band. HRTEM images show that $SrFe_{12}O_{19}$ has a rod structure and has average particle size ranging from 50 to 100 nm. The coercivity value increased by increasing the weight% of nanofiller as it increased from 421 Oe for $SrFe_{12}O_{19}$ to 4502.6 and 4488.2 Oe for x = 3 wt% and 7 wt% for $SrFe_{12}O_{19}$. The transition between the top of the valance band and the bottom of the conduction band in CS/PVP/ x Wt % $SrFe_{12}O_{19;}$ x = 1, 3, 5, 7 system occurred through the indirect transition.

Keywords Chitosan · PVP · $SrFe_{12}O_{19}$ · XRD · IR · TEM, FESEM · VSM · optical

1 Introduction

Chitosan (CS) is considered the second rich natural cationic polysaccharide made from incomplete deacetylation of chitin. It consists of β-(1,4)-2-acetamino-2-deoxy-Dglucose and β-(1,4)-2- amino-2-deoxy-D-glucose [1], and a large quantity of amino and hydroxyl groups which facilitate the formation of strong contact with nanoparticles or different polymer chains to create a new blend with enhanced properties [2]. Chitosan film has unlimited potential for use in different applications such as the food industry as well as packaging material owing to its antimicrobial activity [3]. However, its uses are presently limited because of its high price compared to plastics and darkening through storage at

high temperatures [4]. The blending of CS with synthetic or natural polymers is a simple way to create new materials. The films created by mixing two polymers commonly result in modified mechanical and physical properties related to films prepared of the primary components [5]. Different polymers may interact with CS polymer chains to create an "alloy-like" complex structure, while nanoparticles act as a new crosslinking nod in the polymeric network [6]. Poly vinyl pyrrolidone (PVP) is a hydrophilic polymer produced from N-vinyl pyrrolidone monomer polymerization [7, 8]. PVP has an advantage in various fields as drug delivery applications owing to its good biodegradability and biocompatibility [9], tissue engineering, antibacterial material [10], and catalysis [11]. It was found that the integration of PVP with other polymers is enhancing the swelling, and thermal stability properties [12]. Hence, CS and PVP are perfectly well-matched in the polymeric matrix. The hydrogen bond attraction between carbonyl groups related to PVP and the hydroxyl and amino groups of CS makes the polymers to be miscible[13], leading to the formation of an innovative homogenous biocompatible blend, which may be used for different applications [14]. Further, to improve their inclusive properties, the nanoparticle was added to the polymeric

✉ Rania Ramadan
rramadan@sci.cu.edu.eg

A. M. Ismail
asmaanrc@yahoo.com

[1] Materials Science Lab (1), Physics Department, Faculty of Science, Cairo University, Giza, Egypt

[2] Spectroscopy Department, National Research Centre, 33 El Bohouth Street, Dokki 12622, Giza, Egypt

matrix to form a new composite film consisting of chitosan/poly vinyl Pyrrolidone/nanoparticles film. Hexaferrite M-type hexaferrites has the formula of $MeFe_{12}O_{19}$ (Me = Sr, Pb or Ba) is considered one of the most essential materials depending on their uses in varied applications as permanent magnets and recording media [15, 16], owing to their great magnetic uniaxial anisotropy, high permeability, and low-eddy current loss [17]. The net moment in hexaferrite is produced from the occupation of Fe^{3+} ions the crystallographic positions in three octahedral (FeO_6) sites and one tetrahedral (FeO_4) in addition to trigonal bipyramidal (FeO_5) sites [18–20]. In the present research paper, we discussed the characteristics and physical properties of the film made from chitosan with synthetic polymer (PVP) and compared this film with chitosan/PVP/x Sr-hexaferrite films with different ratios of nanoparticles while the same quantity of PVP and CS polymers.

2 Experimental Technique

2.1 Materials

Strontium nitrate $[Sr(NO_3)_3 6H_2O]$, iron nitrate $[Fe((NO_3)_3 9H_2O]$, Citric acid $[C_6H_8O_7]$, PVP[Poly vinyl pyrrolidone] and (CS) chitosan polymers were obtained from LOBA, India.

2.2 Preparation of Sr-hexaferrite

Sr-hexaferrite has been prepared by using the citrate auto-combustion method as mentioned in our previous work in [21] by mixing the proper quantity of strontium nitrate and iron nitrate according to their stoichiometric ratios with Citrate acid using small amount from distilled water. Then pH of the obtained solution was adjusted to 7. After that, the temperature was set at 200 °C and waiting for all fumes to end, finally, the obtained powder was calcined for 6 h at 900 °C.

2.3 Preparation of CS/PVP/x $SrFe_{12}O_{19}$ Nanocomposites

2.5 gm CS solution was prepared by dissolving in a solution composed of distilled water and acetic acid and stirring at 70 °C (solution A). Solution B was prepared by dissolving 2.5 gm of PVP in 100 ml distilled water. After that solution B was added to solution A under continuous stirring at 70 °C until getting a homogenous solution. The prepared Sr-hexaferrite was added to the prepared blend with different weight percentages (1, 3, 5 and 7 wt%). The resultant nanocomposite solution was sonicated very well using a dip sonicator to be sure the complete dispersion of nanoparticles in CS/PVP

solution. Finally, the nanocomposite solutions were cast into a petri dish and left to dry at 45 °C for 48 hours.

2.4 Measurement Techniques

The chemical structures of $SrFe_{12}O_{19}$, PVP/CS, and PVP/CS/$SrFe_{12}O_{19}$ were confirmed by X-ray diffraction (XRD) [PANalyticalX'Pert Pro target Cu-K] and Fourier transform infrared spectrometer [FTIR] in the range between 400:4000 cm^{-1}. The microstructure and particle distribution were examined by high resolution transmission electron microscope (HRTEM) [JEM-2100 F electron microscope using accelerating voltage of 200 kV]. The surface morphology of samples was observed by using the field emission scanning electron microscopy [FESEM], model (Quanta 250 FEG). Magnetic properties were studied by using a vibrating sample magnetometer (VSM)[Lake Shore VSM 7410] while the optical properties were investigated by UV-Vis absorption [Jasco UV- Vis (V-630)] in wavelength range between 190:1000 nm.

3 Results and Discussion

3.1 XRD

Figure 1 displays XRD pattern of $SrFe_{12}O_{19}$, CS/PVP blend and CS/PVP/x $SrFe_{12}O_{19}$; x=(1, 3, 5 and 7) wt%. For $SrFe_{12}O_{19}$, all the diffraction peaks related to 2theta values 30.33°, 34.148°, 37.12°, 42.52°,and 56.82° have d-spacing values (2.944, 2.622, 2.42020, 2.124, and 1.6190) A° respectively and in agreement with ICDD card number [00-033-1340]. These previous values confirm the formation of single phase without any impurities M-type hexaferrite with space group $P63/mmc$ [22]. The amorphous structure of chitosan is represented by halo peaks at $2\theta=9.1°$, 11.6°, 19.3°, and 22.0° [23]. While PVP has two diffraction peaks at $2\theta = 10.4°$ and 21.2 ° [24]. For CS/PVP blend, there is diffraction peaks are observed at $2\theta=8.5°$, 11.5°, 18.2° and 22.8° which comprises the structural characteristics of the two polymers with shifting in the diffraction peaks which affirmed the interaction between both polymers [25]. By mixing CS with PVP leads to strong interactions between (N–H and O–H) groups of CS and (O–H) group of PVP, consequently the length of inter and intramolecular hydrogen bonds decreased while the PVP and CS become miscible and the film stiffness increased. The semi-crystalline nature of CS/PVP is affected by the addition of Sr-hexaferrite as seen in the peak intensity is decreased by the addition of Sr-hexaferrite. Also, the peak broadening increases which indicated the increase in the amorphous character of the blend. It is noticed that there is shifting in the peak at $2\theta=8.5°$, 11.5° and 22.8°. With increasing Sr-hexaferrite weight%, there is
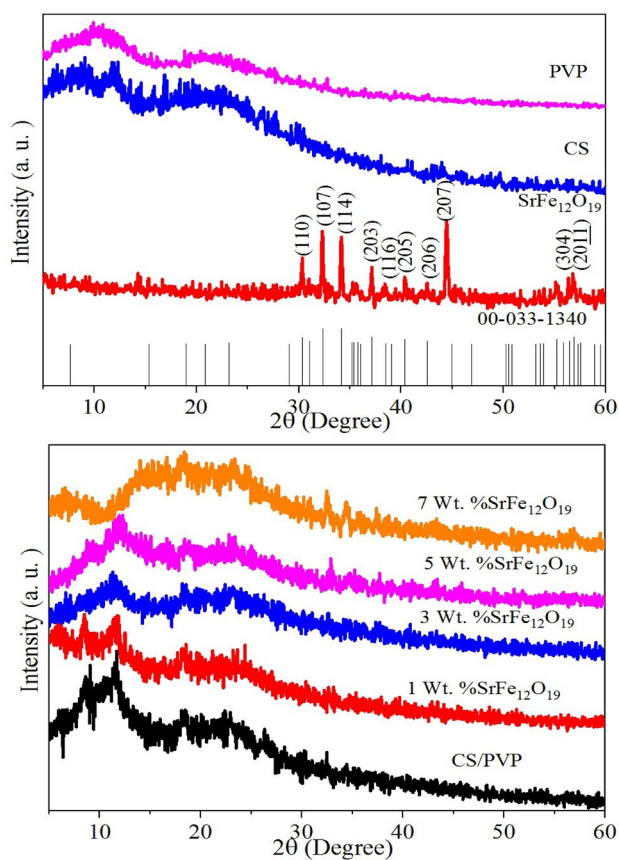
Fig. 1 XRD pattern of SrFe$_{12}$O$_{19}$, CS/PVP blend and CS/PVP/x Wt. %SeFe$_{12}$O$_{19}$ nanocomposite film

Fig. 2 FTIR spectra for CS, PVP, SrFe$_{12}$O$_{19}$, CS/PVP and CS/PVP/ xSrFe$_{12}$O$_{19}$; (x=, 1, 3, 5 and 7) wt. % nanocomposite film

peak appeared at 2θ = 32.4° and 34.5° which are related to the diffraction peak of Sr-hexaferrite. All the above conculsions indicated the change in the crystal structure of CS/PVP by the addition of Sr-hexaferrite. The average crystallite size attributed to Sr-hexaferrite was given by Debye–Scherrer relation [25]:

$$D = \frac{0.9\lambda}{\beta cos\theta} \tag{1}$$

where λ represents the X-ray wavelength, and β donates the full width at half-maximum. The crystallite size for SrFe$_{12}$O$_{19}$ was 44 nm, which indicates the formation in the nanoscale.

3.2 FTIR

FTIR technique provides information about the chemical structure and molecular bonding of investigated samples to confirm their preparation. Figure 2 a reveals the FTIR spectrum related to SrFe$_{12}$O$_{19}$ nanoparticles in the range from 3500 to 370 cm^{-1}. As shown in Fig. 2, a two main
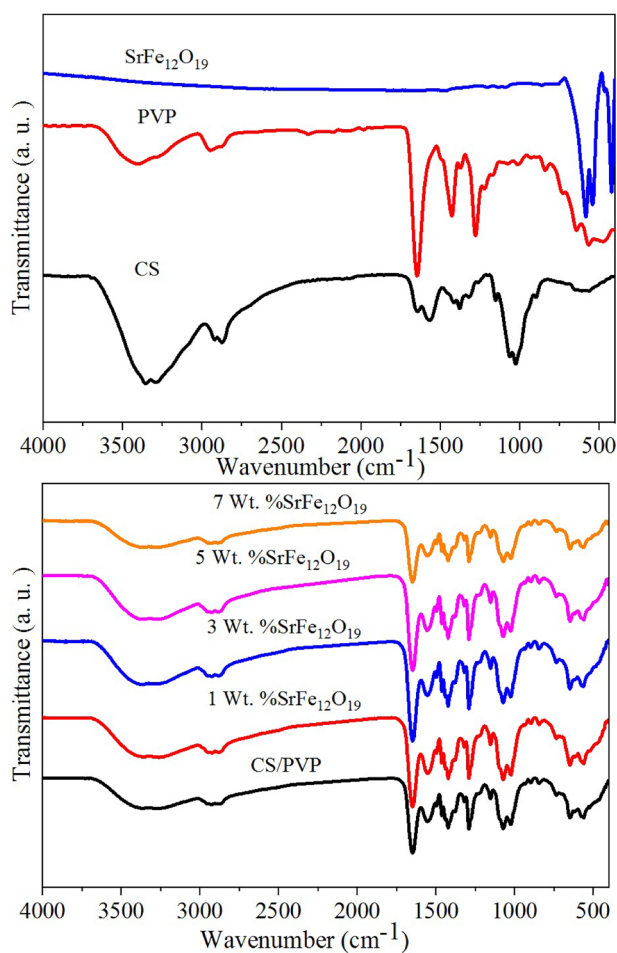
characteristic bands for hexaferrite appeared around 421 and 542 cm^{-1} are assigned to the Fe–O bond corresponding to octahedral and tetrahedral sites respectively [26]. The frequency band at 583 cm^{-1} confirms the formation of Sr hexaferrite in a single phase, as it is associated with Metal-O stretching mode [27]. The absorption band at 885 cm^{-1} may be referred to stretching vibration belonging to the traces of nitrate ion [28]. The band appears at 1098 cm^{-1} corresponding to Sr–O–Sr band. The absorption band observed at 1643 cm^{-1} associates with O–H group stretching vibration [29]. FTIR is also considered an essential technique for identifying the interaction that occurs between any two polymers. For Chitosan, The O–H and N–H groups stretching vibrations are observed at 3360 cm^{-1} and 3286 cm^{-1}. The C–H symmetric and asymmetric stretching vibrations are seen at 2921 cm^{-1} and 2870 cm^{-1}, respectively. The amide I and amide II bond vibrations are assigned at 1641 cm^{-1} and 1564 cm^{-1}, respectively. The primary alcoholic OH group is observed at 1382 cm^{-1}. At 1155 cm^{-1}, the stretching vibration of the bridge oxygen in glycosidic bonds is observed.

The C–O stretching vibration is seen at 1063 cm^{-1} and 1027 cm^{-1}. The C–H bending vibration is assigned at 896 cm^{-1} [30, 31]. In PVP spectrum, the O–H stretching vibration is observed at 3408 cm^{-1}. The asymmetric and symmetric stretching vibrations of CH_2 are located at 2945 cm^{-1} and 2883 cm^{-1}, respectively. The C–O stretching vibration is observed at 1646 cm^{-1}. Bands at 1427 cm^{-1} and 1373 cm^{-1} are assigned to the bending vibrations of the CH group. The band located at 1278 cm^{-1} is assigned to the C–N bending vibration. The twisting and rocking vibrations of CH_2 are assigned at 1223 cm^{-1} and 1012 cm^{-1}. The N–C=O bending vibration is located at 567 cm^{-1} [32, 33].

For CS/PVP spectrum, it is observed that the complexation between CS and PVP is confirmed through the change in the position and band broadening of OH and NH bands of individual polymers in the blend. Also, there is a shift in the amide II band and C–O band of chitosan. Also, the C–N band position of PVP is shifted toward a higher frequency. Also, there is a change in the band intensity. This result affirmed the homogeneity and interaction between CS and PVP.

For CS/PVP/x Wt% $SrFe_{12}O_{19}$; (x = 1, 3, 5 and 7), it is observed that there is a change in intensity of all bands with the addition of $SrFe_{12}O_{19}$. Also, it is noticed that the broadening of the band at 3259 cm^{-1} increases. This confirmed the interaction between CS/PVP polymer and $SrFe_{12}O_{19}$.

3.3 Morphological Study

Electron micrographs of TEM and SEM were used to estimate the distribution of $SrFe_{12}O_{19}$ nanoparticles in CS/PVP matrix with its crystallographic and morphological features. Consequently, to investigate the morphology and homogenous distribution of Sr-hexaferrite nanoparticles in CS/PVP blend matrix, transmission and scanning electron micrographs have been obtained in Figs. 3 and 4. Figure 3 a presents HRTEM for $SrFe_{12}O_{19}$ nanoparticles, it has a clear rod structure and furthermore, the selected area of electron diffraction (SAED) confirms the crystallinity of the

nanopowder, as it is matched with data obtained from XRD. The histogram of prepared samples gives information about the particle size distribution of Sr-hexaferrite and found that it has an average particle size ranging from 50 to 100 nm.

Figure 4 shows SEM micrographs of CS/PVP blend, CS/PVP/3 wt% $SrFe_{12}O_{19}$ and CS/PVP/7 wt% $SrFe_{12}O_{19}$. Figure 4 a Surface morphology of CS/PVP blend is smooth and no cracks are observed, signifying that CS/PVP blend has a compatible structure. After incorporating 3 and 7 wt% of $SrFe_{12}O_{19}$, the film surfaces become rougher. Also, there are white clusters agglomerated and distributed on the surface of CS/PVP blend.

3.4 Magnetic Study

Knowing about the magnetic behavior, hysteresis loops at room temperature using external field variable from 0 to 20 kOe, as shown in Fig. 5a, b. The information about the magnetic properties such as saturation magnetization (M_s), Coercivity (H_c), remanence magnetization (M_r), squareness ratio (M_r/M_s), Exchange bias (H_{EB}) and area of hysteresis loop were obtained from M-H curve and listed in Table 1. The exchange bias is calculated by the following equation [34].

$$H_{EB} = \frac{-[H(-) + H(+)]}{2} \tag{2}$$

where H(−) and H(+) are the magnetization's intercepts with the −ve as well as +ve along the field axis, respectively. While the area of the hysteresis loop of any substance that represents energy loss during magnetization. The area of hysteresis loop is obtained by Just Identify the forward and backward parts of the hysteresis loop by looking at where the difference in x value in the tuple (x,y) switches from being positive to negative or vice versa. Then basically subtract the area under the two curves.

Figure 5 a shows a direct relation between magnetization and applied magnetic field owing to the alignment of dipoles

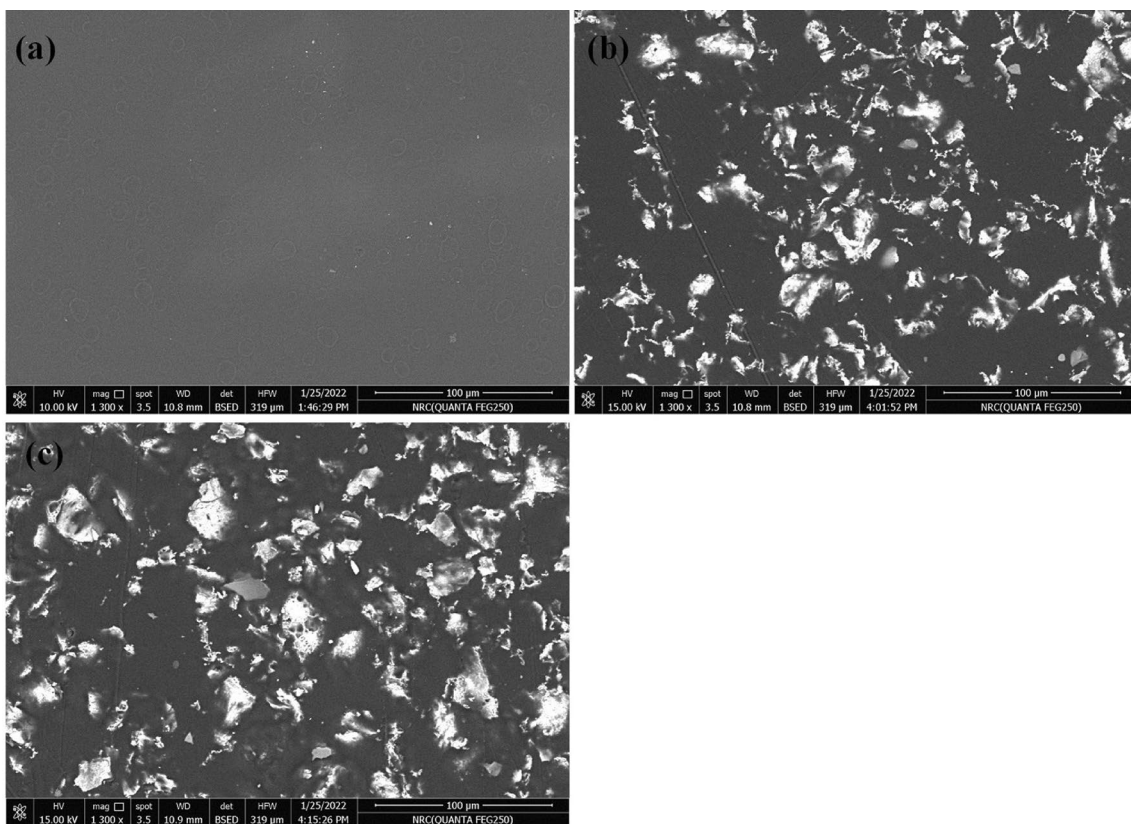**Fig. 3 a** TEM micrographs and **b** histogram of SrFe12O19
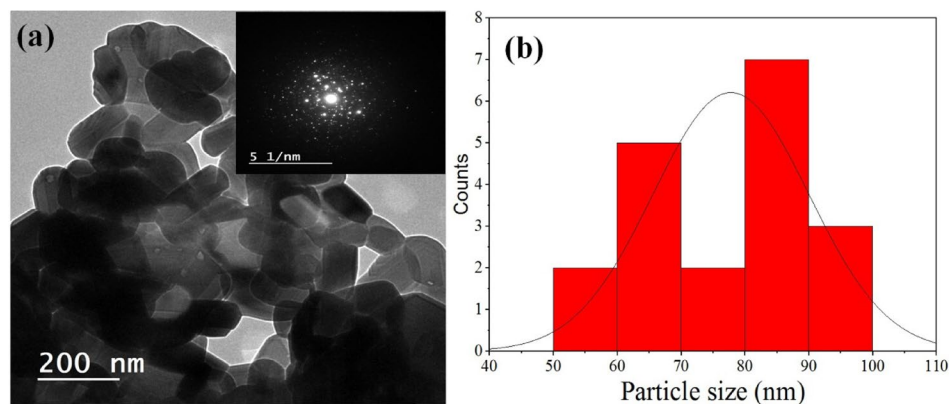
Fig. 4 SEM micrographs of **a** CS/PVP blend, **b** CS/PVP/3Wt% SrFe$_{12}$O$_{19}$ and CS/PVP/7wt% SrFe$_{12}$O$_{19}$
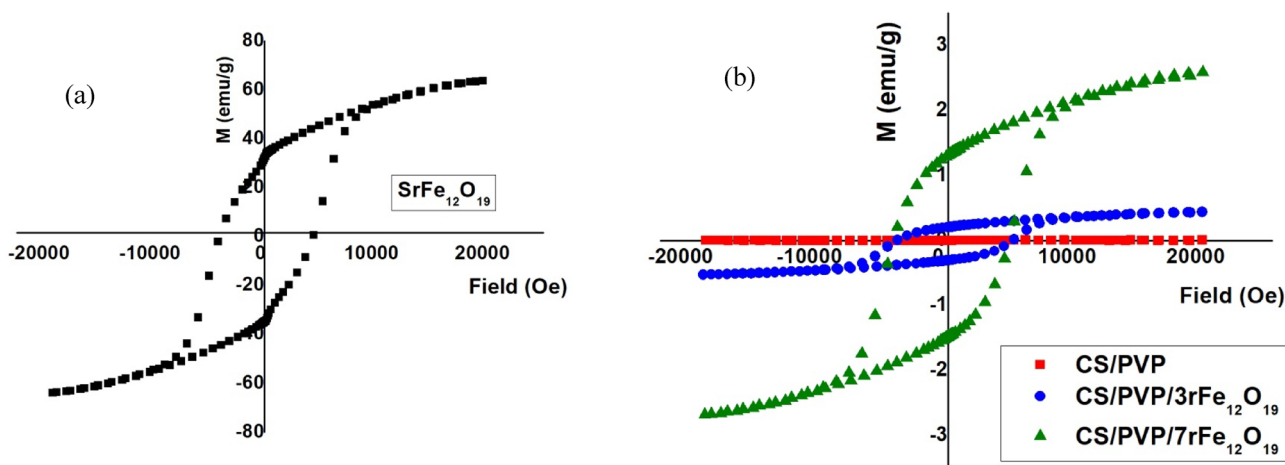
Fig. 5 **a**, **b** VSM of **a** SrFe$_{12}$O$_{19}$, **b** CS/PVP blend, CS/PVP/3wt% SrFe$_{12}$O$_{19}$ and CS/PVP/7wt% SrFe$_{12}$O$_{19}$

(Fe^{2+} and Fe^{3+}) with the direction of the applied field and there is no saturation state and this is a characteristic feature for M-type hexaferrite, therefore, we considered the saturation magnetization to be the magnetization value corresponding to the highest value of the applied field [34]. Following is how we

have evaluated Ms using the empirical law of approach (LAS) to saturation for materials cannot reach to saturation [34].
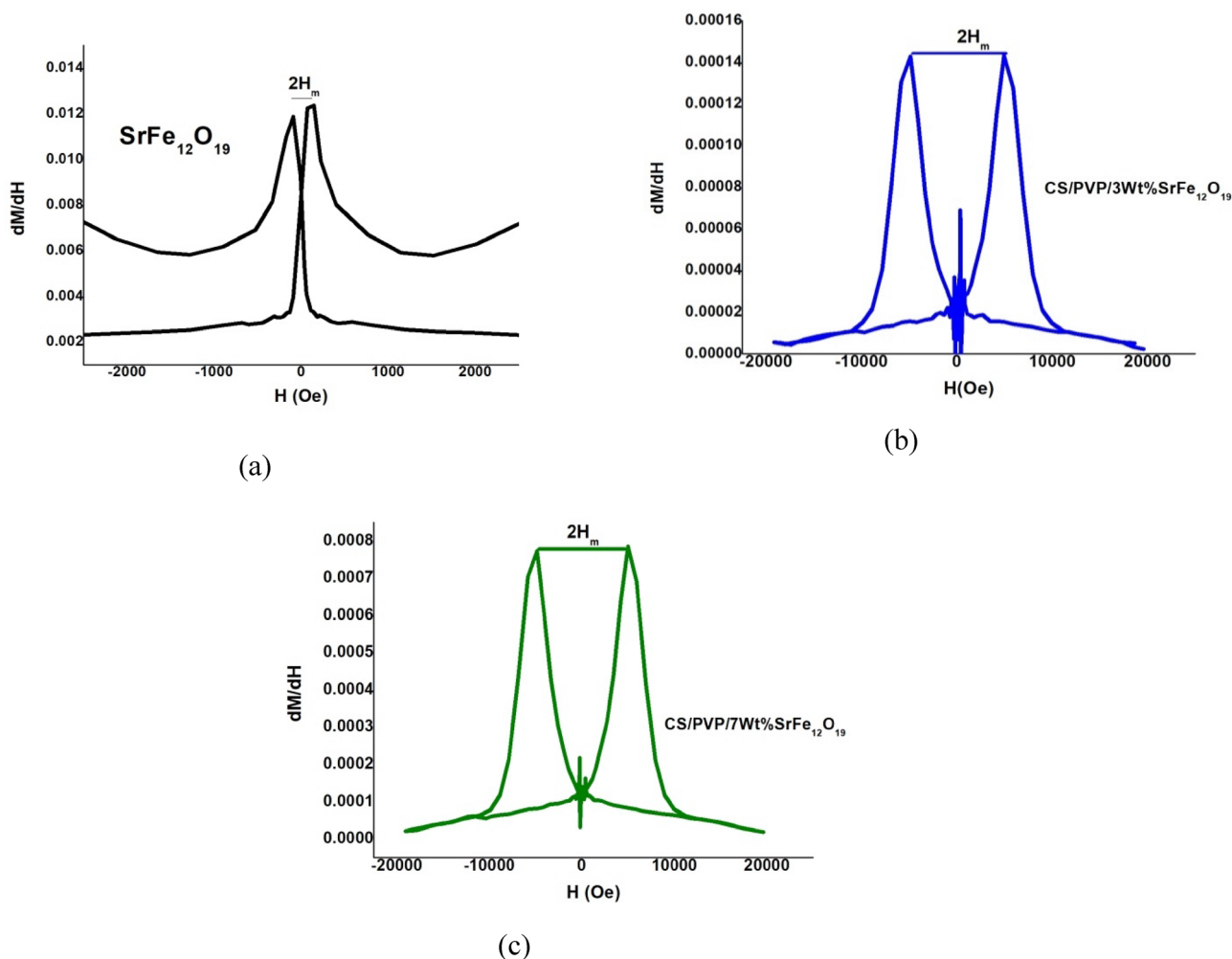
$$M = M_s\left(1 - \frac{b}{H^2}\right) + \chi H \tag{3}$$

(a)

(b)

(c)

Fig. 6 **a–c** First derivatives of magnetization for **a** $SrFe_{12}O_{19}$, **b** CS/PVP/3Wt% $SrFe_{12}O_{19}$ and **c** CS/PVP/7Wt% $SrFe_{12}O_{19}$

where χ is the susceptibility at high fields and b is related to magnetocrystalline anisotropy. We obtained the Ms, b, and data by fitting the M(H) data for fields higher than 7 kOe. It gives a straight line, the intercept of which (with the M-axis) gives the saturation magnetization, and the slope of which gives the magneto-crystalline anisotropy constant. For χ its values are negligible and ignorable.

When $SrFe_{12}O_{19}$ inclusion through CS/PVP matrix, the samples CS/PVP/3 Wt% $SrFe_{12}O_{19}$ and CS/PVP/7 Wt% $SrFe_{12}O_{19}$ still considered as hard magnetic materials because of their large magnetic hysteresis loop, although we observed that the values of the saturation magnetization dropped from 63.8 emu/g to 0.44 and 2.59 emu/g for CS/PVP/3 Wt% $SrFe_{12}O_{19}$ and CS/PVP/7 Wt% $SrFe_{12}O_{19}$ respectively. Remnant magnetization followed the same trend as saturation magnetization and decreased from 33.9 emu/g for $SrFe_{12}O_{19}$ to 0.480 and 2.6357 emu/g for CS/PVP/3Wt% $SrFe_{12}O_{19}$

and CS/PVP/7Wt% $SrFe_{12}O_{19}$ respectively. these could be explained by the non-magnetic nature of CS/PVP matrix as seen in Fig. 5, b however, sustained the magnetic characteristic after adding the nanoparticles into CS/PVP film existing by the $SrFe_{12}O_{19}$. The value of coercivity (H_c) donates information about the magnetic field strength used to demagnetize the magnetic material and it depends on changing the porosity, and morphology as well as magneto crystalline anisotropy [35]. Herein, the coercivity value increased by increasing the weight% of nanofiller as it increased from 421Oe for $SrFe_{12}O_{19}$ to 4502.6 and 4488.2 Oe for x = 3% and 7%. This is attributed to the CS/PVP blend which increases the magnetic anisotropy and consequently the coercivity increased. The values of the squareness ratios (ratio between remanence and saturation magnetization) for $SrFe_{12}O_{19}$, CS/PVP/3Wt% $SrFe_{12}O_{19}$ and CS/PVP/7Wt% $SrFe_{12}O_{19}$ donate values significantly higher than 0.5, showing that the samples have hard

Table 1 Magnetic parameters, containing saturation magnetization ($M_s(+)$, $M_s(−)$ and M_s), coercive field (Hc), remnant magnetization (($M_r(+)$, $M_r(−)$ and M_r), squareness ratio (M_r/M_s), Coercivity (($H_c(+)$, $H_c(−)$ and H_c) and H_c), exchange bias field (H_{EB}), and the area of the hysteresis loop area for $SrFe_{12}O_{19}$, CS/PVP blend, CS/PVP/3Wt% $SrFe_{12}O_{19}$ and CS/PVP/7Wt% $SrFe_{12}O_{19}$.

$SrFe_{12}O_{19}$ Wt%	M_s (+) emu/g	M_s (−) emu/g	M_s emu/g	M_r (+) emu/g	M_r (−) emu/g	M_r emu/g	M_r/M_s	H_c (+) (Oe)	H_c (−) (Oe)	H_c (Oe)	H_{EB} (Oe)	Area erg/g $\cdot 10^3$
100	65.69	− 65.69	65.69	33.9	− 34	33.9	0.53	421	− 4198	4204.3	6	639.6
0	5.4E-3	− 5.4E-3	5.4E-3	334E-6	− 465.4E-6	399.7E-6	73.9E- 3	345.3	− 351.4	3.04	3	0.07
3	0.44	− 0.52	0.48	0.21	− 0.30	0.26	0.53	4850	− 4155	4502.6	347	5.34
7	2.59	− 2.68	2.64	1.33	− 1.46	1.39	0.53	4576.7	− 4399.7	4488.2	89	29.19

magnetic behavior [36]. Another magnetic parameter that was calculated is the area of the hysteresis loop, which is defined as the quantity of energy required to magnetize and demagnetize every cycle. As listed in Table 1, the area of the hysteresis loop has its lowest value for pure CS/PVP matrix and increased by increasing the weight% of $SrFe_{12}O_{19}$ inside CS/PVP matrix, due to the non-magnetic nature of CS and PVP polymers.

Other magnetic parameters were calculated and listed in Table 2 such as anisotropy constant (K) and anisotropy field (H_a). These values were calculated by using the following relations [37–39]:

$$K = \frac{[H_c \times M_s]}{0.96} \quad (4)$$

$$H_a = \frac{2K}{M_s} \quad (5)$$

The magnetic anisotropy constant gives information related to the struggle of dipoles for undergoing annihilation by using a reverse applied magnetic field. As seen in Table 2, the highest values of K and H_a are associated with pure nanoparticles, and these values decrease by decreasing the weight% of nanofiller mixing into CS/PVP matrix. The magnetic susceptibility dM/dH could be calculated through Fig. 6a-c at room temperature, which explains the response of the material when it is exposed to a magnetic field. Thus the largest value is 12 and it is observed for $SrFe_{12}O_{19}$ as it is expected due to its high magnetic properties and this magnetic response is decreased after adding the nonmagnetic CS/PVP blend. While pure CS/PVP blend did not show any response to the magnetic field due to its non-magnetic nature as discussed above.

We concluded that varying in the values of the magnetic parameters associated with changing the weight% of the nanofiller included in the polymeric matrix. Owing to the nature of coating polymers as well as the surface defects as cracks and pores which are related to nano filler.

3.5 Optical Properties

The optical measurement is used to calculate the energy gap materials as well as determine the nature of the band gap. The absorption depends on the electron excitation between the valance band and the conduction band [40]. In this study, all samples displayed absorbance peaks around a wavelength of 250 nm as shown in Fig. 7. By increasing the weight% of $SrFe_{12}O_{19}$, the absorbance increased. This may be explained by the complexation between CS/PVP blend and $SrFe_{12}O_{19}$ nanoparticles. The electron excitation from lower to higher energy state due to the incident of the photon, these phenomena defined as the absorption edge and it is given by extrapolating the straight part of the absorption coefficient

Table 2 The values of magnetic anisotropy constant, anisotropy field, H_m and dM/dH of $SrFe_{12}O_{19}$, (b) CS/PVP blend, CS/PVP/3Wt% $SrFe_{12}O_{19}$ and CS/PVP/7Wt.% $SrFe_{12}O_{19}$

Composition	$K \cdot 10^3$ (erg/g)	Ha (Oe)	H_m (Oe)	$\frac{dM}{dH}$(emu/g Oe) $\cdot 10^{-3}$	
				$H \rightarrow 0$	$H \rightarrow H_m$
$SrFe_{12}O_{19}$	28.8	877	112	8	12
CS/PVP blend,	0.017	6283	–	–	–
CS/PVP/3Wt% $SrFe_{12}O_{19}$	2.25	1679	5000	0.00002	0.00014
CS/PVP/7Wt% $SrFe_{12}O_{19}$.	12.32	8746	4927	0.0001	0.0007
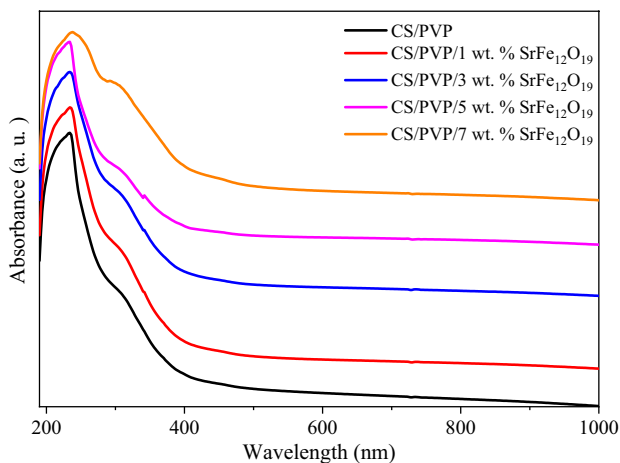
Fig. 7 UV–Vis spectra of CS/PVP blend and CS/PVP/x$SrFe_{12}O_{19}$ nanocomposite film
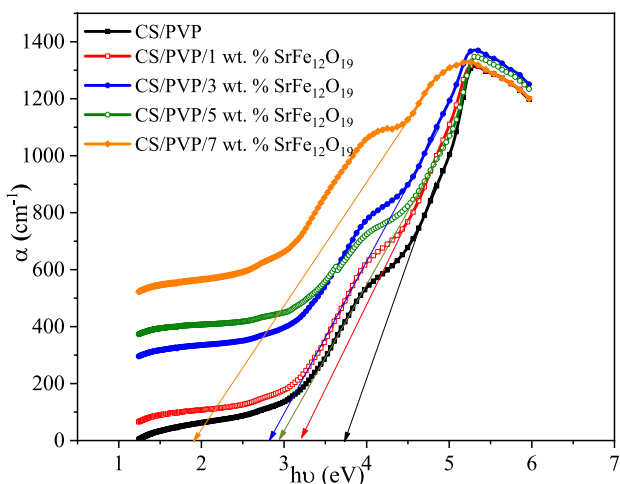
Fig. 8 Absorption coefficient as a function of the photon energy of CS/PVP blend and CS/PVP/x$SrFe_{12}O_{19}$ nanocomposite film

(α) and photon energy (hυ) [41]. The absorption coefficient is given by.

$$\alpha = \frac{2.303A}{d} \tag{6}$$

where; A represents the absorbance, and d donates the sample thickness.

It is observed from Fig. 8 and the date mentioned in Table 3. The absorption edge is decreased by increasing the weight% of the nanofiller owing to the existence of the localized states in the band gap leading to the final number of the state in the system being changed. By using Tauc's plot relation [42], the energy band gap could be calculated through the following equations:

$$(\alpha h\upsilon) = B \left(h\upsilon - E_g\right)^n \tag{7}$$

where α donates the absorption coefficient, B is constant, h gives the photon energy and n = 1/2 or 2 for direct and indirect transition respectively between the valence and conduction bands.

We concluded two facts from Fig. 9. First one related to the value of energy band gap which is reduced by increasing the weight% of $SrFe_{12}O_{19}$ nanoparticles for both the direct and indirect transitions due to the formation of new energy state in the band gap region which related to the interaction between CS/PVP blend and nanofiller. Furthermore, the values of the energy band gap are listed in Table 3 and as it is observed the energy band gap associated to the indirect transition is lower than that observed for the direct transition which indicates that the transition between the top of the valance band and the bottom of the conduction band in CS/PVP/x Wt.% $SrFe_{12}O_{19}$; x = 1, 3, 5, 7 system occurred through the indirect transition.

4 Conclusion

CS/PVP blend doped by four concentrations of Sr-hexaferrite films have been synthesized successfully. The results related to XRD and FTIR approved the interaction between CS/PVP blend and nanofiller. The surface morphology changed by the addition of $SrFe_{12}O_{19}$ by the appearance of white spots distributed on the surface of CS/PVP blend which means that the roughness increases. The values of the squareness ratios (ratio between remanence and saturation magnetization) for $SrFe_{12}O_{19}$, CS/PVP/3Wt% $SrFe_{12}O_{19}$ and CS/PVP/7Wt% $SrFe_{12}O_{19}$ donate values significantly higher than 0.5, showing that the samples
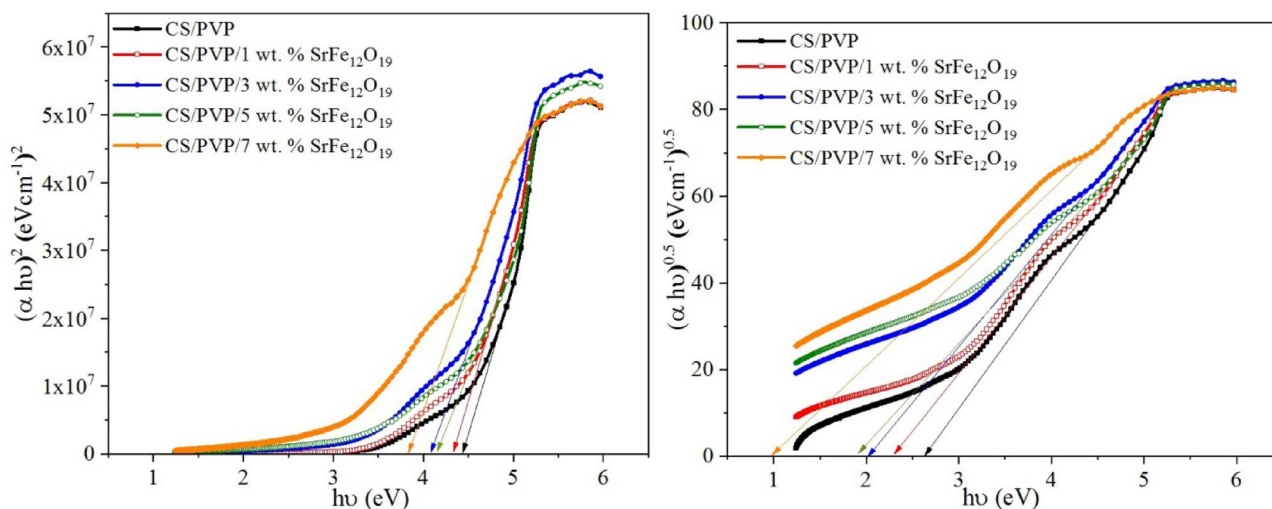
Fig. 9 The variation of $(\alpha h\upsilon)^2$ and $(\alpha h\upsilon)^{0.5}$ versus $h\upsilon$ of CS/PVP blend and CS/PVP/xSrFe$_{12}$O$_{19}$ nanocomposite film

Table 3 Values of Absorption edge, direct and indirect band gap for CS/PVP/$x$wt% SrFe$_{12}$O$_{19}$; $x = 1, 3, 5, 7$ system

SrFe$_{12}$O$_{19}$ Wt%	Absorption edge (eV)	Direct band gap (eV)	Indirect band gap (eV)
0	3.72	4.43	2.65
1%	3.21	4.34	2.30
3%	2.84	4.07	2.03
5%	2.94	4.15	1.92
7%	1.93	3.83	0.99

have hard magnetic behavior. The optical parameters have been enhanced by the inclusion of Sr-hexaferrite into CS/PVP polymeric matrix as the absorption edge and energy band gap values decreased which enable these prepared films suggested for the optical applications.

Author Contributions RR and AMI wrote the main manuscript text, prepared all figures and reviewed the manuscript.

Data Availability Data sharing not applicable to this article as no datasets were generated or analyzed during the current study.

Declarations

Competing interests The authors declare no competing interests.

References

1. A. Naskar, S. Lee, K.S. Kim, Antibacterial potential of Ni-doped zinc oxide nanostructure: comparatively more effective against Gram-negative bacteria including multi-drug resistant strains. RSC Adv **10**(3), 1232–1242 (2020)
2. E.G. Lemraski, H. Jahangirian, M. Dashti, E. Khajehali, S. Sharafinia, R. Rafiee-Moghaddam, T.J. Webster, Antimicrobial double-layer wound dressing based on chitosan/polyvinyl alcohol/copper: in vitro and in vivo assessment. Int. J. Nanomed **16**, 223 (2021)
3. S.P. Miguel, A.F. Moreira, I.J. Correia, Chitosan based-asymmetric membranes for wound healing: a review. Int. J. Biol. Macromol **127**, 460–475 (2019)
4. A.M. Ismail, R. Ramadan, M.M. El-Masry (2023). The role of nanoparticles inclusion in monitoring the physical properties of PVDF. Journal of the Australian Ceramic Society, 53: 333-341
5. R. Ramadan, Study the multiferroic properties of BiFeO3/Ni0.1Fe2.9O4 for heavy metal removal. Appl. Phys. A **129**(2), 125 (2023)
6. D. Archana, B.K. Singh, J. Dutta, P.K. Dutta, Chitosan-PVP-nano silver oxide wound dressing: in vitro and in vivo evaluation. Int. J. Biol. Macromol **73**, 49–57 (2015)
7. M. Slaný, Ľ Jankovič, J. Madejová, Structural characterization of organo-montmorillonites prepared from a series of primary alkylamines salts: Mid-IR and near-IR study. Appl. Clay Sci **176**, 11–20 (2019)
8. M.S. Gaafar, S.Y. Marzouk, I.S. Mahmoud, A.M.A. El-Aziz, M. Afifi, Influence of samarium on some acoustical, physical

and radiation shielding characteristics of Bi 2 O 3–ZnO–PbO glasses. J. Mater. Sci.: Mater. Electron **31**, 21502–21514 (2020)

9. Y.S. Choi, Q. Jing, A. Datta, C. Boughey, S. Kar-Narayan, A triboelectric generator based on self-poled Nylon-11 nanowires fabricated by gas-flow assisted template wetting. Energy Environ. Sci **10**(10), 2180–2189 (2017)

10. S.V. Kostromin, A. Podshivalov, M. Asandulesa, S. Bronnikov (2019, October). Electrical conductivity of polyazomethine/reduced graphene oxide nanocomposites. In IOP Conference Series: Materials Science and Engineering (Vol. 634, No. 1, p. 012005). IOP Publishing

11. M.M. El-Masry, R. Ramadan, Enhancing the properties of PVDF/MFe2O4;(M: Co–Zn and Cu–Zn) nanocomposite for the piezoelectric optronic applications. J. Mater. Sci.: Mater. Electron **33**(19), 15946–15963 (2022)

12. R. Ramadan, M.K. Ahmed, Impact of adding vanadium pentoxide to Mn-doped magnetite for technological uses. Appl. Phys. A **128**(12), 1056 (2022)

13. R. Poonguzhali, S.K. Basha, V.S. Kumari, Fabrication of asymmetric nanostarch reinforced Chitosan/PVP membrane and its evaluation as an antibacterial patch for in vivo wound healing application. Int. J. Biol. Macromol **114**, 204–213 (2018)

14. J. Rezaie, A. Akbari, V. Rahimkhoei, Z.M. Lighvani, H. Jafari (2021). Halloysite nanotubes/carbohydrate-based hydrogels for biomedical applications: from drug delivery to tissue engineering. Polymer Bulletin, 79: 4497-5413

15. L. Ma, X. Shi, X. Zhang, L. Li, Electrospinning of polycaprolacton/chitosan core-shell nanofibers by a stable emulsion system. Colloids Surf., A **583**, 123956 (2019)

16. I.R. Serra, R. Fradique, M.C.D.S. Vallejo, T.R. Correia, S.P. Miguel, I.J. Correia, Production and characterization of chitosan/gelatin/β-TCP scaffolds for improved bone tissue regeneration. Mater. Sci. Engineering: C **55**, 592–604 (2015)

17. X.Y. Dai, W. Nie, Y.C. Wang, Y. Shen, Y. Li, S.J. Gan, Electrospun emodin polyvinylpyrrolidone blended nanofibrous membrane: a novel medicated biomaterial for drug delivery and accelerated wound healing. J. Mater. Science: Mater. Med. **23**, 2709–2716 (2012)

18. M. Contardi, D. Kossyvaki, P. Picone, M. Summa, X. Guo, J.A. Heredia-Guerrero, … I.S. Bayer, Electrospun polyvinylpyrrolidone (PVP) hydrogels containing hydroxycinnamic acid derivatives as potential wound dressings. Chem. Eng. J **409**, 128144 (2021)

19. S.A. Al Kiey, R. Ramadan, M.M. El-Masry, Synthesis and characterization of mixed ternary transition metal ferrite nanoparticles comprising cobalt, copper and binary cobalt–copper for high-performance supercapacitor applications. Appl. Phys. A **128**(6), 473 (2022)

20. V. Rania Ramadan, M.M. Uskoković, El-Masry (2023). Triphasic CoFe2O4/ ZnFe2O4 / CuFe2O4 Nanocomposite for Water Treatment. Journal of Alloys and Compounds. https://doi.org/10.1016/j.jallcom.2023.170040

21. R. Kumar, S. Ranwa, G. Kumar, Biodegradable flexible substrate based on chitosan/PVP blend polymer for disposable electronics device applications. J. Phys. Chem. B **124**(1), 149–155 (2019)

22. J.T. Yeh, C.L. Chen, K.S. Huang, Y.H. Nien, J.L. Chen, P.Z. Huang, Synthesis, characterization, and application of PVP/chitosan blended polymers. J. Appl. Polym. Sci **101**(2), 885–891 (2006)

23. M. Abolhassani, C.S. Griggs, L.A. Gurtowski, J.A. Mattei-Sosa, M. Nevins, V.F. Medina, T.A. Morgan, L.F. Greenlee, Scalable chitosan-graphene oxide membranes: the effect of GO size on

properties and cross-flow filtration performance. ACS omega **2**(12), 8751–8759 (2017)

24. M.A. El-Kader, M.T. Elabbasy, A.A. Adeboye, A.A. Menazea (2021). Nanocomposite of PVA/PVP blend incorporated by copper oxide nanoparticles via nanosecond laser ablation for antibacterial activity enhancement. Polymer Bulletin, 79: 9779-9795

25. M. Abdolrahimi, M. Seifi, M.H. Ramezanzadeh, Study the effect of acetic acid on structural, optical and mechanical properties of PVA/chitosan/MWCNT films. Chin. J. Phys **56**(1), 221–230 (2018)

26. W. Zhang, S. Ke, C. Sun, X. Xu, J. Chen, L. Yao, Fate and toxicity of silver nanoparticles in freshwater from laboratory to realistic environments: a review. Environ. Sci. Pollut. Res **26**, 7390–7404 (2019)

27. X. Zhao, K. Wang, C. Ai, L. Yan, C. Jiang, J. Shi, Improvement of antifungal and antibacterial activities of food packages using silver nanoparticles synthesized by iturin A. Food Packaging and Shelf Life **28**, 100669 (2021)

28. I. Hamed, A.N. Jakobsen, J. Lerfall, Sustainable edible packaging systems based on active compounds from food processing byproducts: a review. Compr. Rev. Food Sci. Food Saf **21**(1), 198–226 (2022)

29. A. Gull, N. Bhat, S.M. Wani, F.A. Masoodi, T. Amin, S.A. Ganai, Shelf life extension of apricot fruit by application of nanochitosan emulsion coatings containing pomegranate peel extract. Food Chem **349**, 129149 (2021)

30. M. Fernandes Queiroz, K.R.T. Melo, D.A. Sabry, G.L. Sassaki, H.A. Rocha O, Does the use of chitosan contribute to oxalate kidney stone formation? Mar. Drugs **13**(1), 141–158 (2015)

31. A.B. Vino, P. Ramasamy, V. Shanmugam, A. Shanmugam, Extraction, characterization and in vitro antioxidative potential of chitosan and sulfated chitosan from Cuttlebone of Sepia aculeata Orbigny, 1848. Asian Pac. J. Trop. Biomed. **2**(1), S334–S341 (2012)

32. D. Kamaruddin, Edikreshna, I. Sriyanti, M. Munir, Khairurrijal. (2017). Synthesis of Polyvinylpyrrolidone (PVP)-Green Tea Extract Composite Nanostructures using Electrohydrodynamic Spraying Technique. IOP Conference Series Materials Science And Engineering, 202, 012043

33. R. Bryaskova, D. Pencheva, S. Nikolov, T. Kantardjiev, Synthesis and comparative study on the antimicrobial activity of hybrid materials based on silver nanoparticles (AgNps) stabilized by polyvinylpyrrolidone (PVP). J. Chem. Biol **4**(4), 185–191 (2011)

34. E.E. Ateia, K. Elsayed, R. Ramadan, Tuning the properties of ba-m hexaferrite BaFe11. 5Co0. 5O19: a road towards diverse applications. J. Inorg. Organomet. Polym Mater **32**(7), 2502–2512 (2022)

35. C. Tanasoiu, P. Nicolau, C. Miclea, Preparation and magnetic properties of high coercivity strontium ferrite micropowders obtained by extended wet milling. IEEE Trans. Magn **12**(6), 980–982 (1976)

36. H. Taguchi, H. Nishio, Y. Yokoyama, F. Hirata, T. Takeishi, T. Mori, Crystal distortion of submicron Sr-ferrite particles by milling. IEEE Translation Journal on Magnetics in Japan **9**(5), 3–8 (1994)

37. S.V. Ketov, Y.D. Yagodkin, A.L. Lebed, Y.V. Chernopyatova, K.J.J.O.M. Khlopkov, Structure and magnetic properties of nanocrystalline SrFe12O19 alloy produced by high-energy ball milling and annealing. J. Magn. Magn. Mater **300**(1), e479–e481 (2006)

38. M. Mai. A. El-Masry, H.Y. El-razek Mahmoudb, Morshidyc, Rania Ramadan, Cu2 + and Zn2 + doped cobalt spinel ferrite:

insights on structural, thermal conduction, magnetic and elastic properties, (2023), https://doi.org/10.1007/s10854-022-09777-3

39. R.S. Hafez, R. Ramadan, S.S. El-Khiyami, Investigation of structural, optical, magnetic, and electrical properties of PMMA doped with magnetite nanoparticles. J. Mater. Sci.: Mater. Electron **32**(11), 14557–14568 (2021)

40. B. Zhang, I. Mahariq, N. Tran, M.Z. Mahmoud, M.N. Akhtar, Enhanced electromagnetic wave dissipation features of magnetic ni microspheres by developing core-double shells structure. Ceram. Int **48**(1), 446–454 (2022)

41. P. Jiang, Q. Xu, N. Tran, A.S. El-Shafay, V. Mohanavel, A. Abdelrahman, M. Ravichandran, Boosted microwave absorption properties of CoFe2O4 with extraordinary 3D morphologies. Ceram. Int **48**(10), 13541–13550 (2022)

42. G. Fan, T. Xiong, A. Mouldi, B. Bouallegue, N. Tran, M.Z. Mahmoud, Enhanced electromagnetic interference shielding effectiveness of h-BN decorated micro cube-like CaTiO3/Cu nanocomposite. Ceram. Int **48**(6), 8529–8539 (2022)